UC Berkeley
UC Berkeley Previously Published Works

Title

Particle Size Optimization of Thermochemical Salt Hydrates for High Energy Density Thermal Storage

Permalink

Journal

ISSN

Authors

Martin, Andrew
Lilley, Drew
Prasher, Ravi
et al.

Publication Date

DOI

Peer reviewed

Particle Size Optimization of Thermochemical Salt Hydrates for High Energy Density Thermal Storage

Andrew Martin,[1] Drew Lilley,[1,2] Ravi Prasher,[1,2] *, Sumanjeet Kaur[1] *

[1]Energy Technologies Area, Lawrence Berkeley National Laboratory. Berkeley, CA, 94701 USA
[2]Department of Mechanical Engineering, UC Berkeley. Berkeley, CA, 94720 USA
E-mail: *Sumanjeet Kaur, skaur@lbl.gov. *Ravi Prasher, rsprasher@lbl.gov.

Thermal energy storage (TES) solutions offer opportunities to reduce energy consumption, greenhouse gas emissions and cost. Specifically, they can help reduce the peak load and address the intermittency of renewable energy sources by time shifting the load which are critical towards zero energy buildings. Thermochemical materials (TCMs) as a class of TES undergo a solid-gas reversible chemical reaction with water vapor to store and release energy with high storage capacities (600 kWh/m^3) and negligible self-discharge that makes them uniquely suited as compact, stand-alone units for daily or seasonal storage. However, TCMs suffer from instabilities at the material (salt particles) and reactor level (packed beds of salt), resulting in poor multi-cycle efficiency and high-levelized cost of storage. In this study, a model is developed to predict the pulverization limit or R$_{crit}$ of various salt hydrates during thermal cycling. This is critical as it provides design rules to make mechanically stable TCM composites as well as enables the use of more energy efficient manufacturing process (solid-state mixing) to make the composites. The model is experimentally validated on multiple TCM salt hydrates with different water content and effect of R$_{crit}$ on hydration and dehydration kinetics is also investigated.

1. Introduction

Scalable, affordable, and sustainable energy storage solutions are required to allow for wider adoption of renewable electricity. So far, many energy storage solutions have been explored for both short- and long-term storage,[1] but the on-site energy storage needs for the building sector are mostly overlooked despite the fact that buildings use 40% of global energy and accounts for approx. 60% consumption of world's electricity which are responsible for 33% of greenhouse gas emissions.[2] Currently the electricity storage technologies such as Li-ion batteries are the most common option for energy storage in buildings, despite the fact that heating and cooling are the major end uses of energy in the building. In fact, it is projected that by 2050 the heating and cooling (thermal loads) will account for more than 50% of the energy demand in buildings and thus storing energy using TES technologies is an attractive alternative to Li-ion batteries as they could provide affordable, sustainable and more energy-efficient solution for on-site energy storage in buildings.[3] In terms of functionality TES can be charged by consuming electricity, then can be discharged as thermal energy during peak hours to displace later electricity use. Furthermore, TES could leverage the effect of diurnal swings or fluctuation in ambient temperature to significantly improve its efficiency as shown by Odukomaiya et al.[3]

TES can be broadly divided into sensible, phase change materials (PCMs) and thermochemical materials (TCMs).[4] TCMs have a fundamental advantage of having significantly higher theoretical energy densities (200 to 600 kWh/m^3) than sensible and latent (50 to 150 kWh/m^3) because the energy is stored in the solid-gas water reaction without any liquid-solid phase change involved (thus differentiating itself from PCMs).[5] For building applications, low charge-discharge temperature is highly desirable in thermal energy storage materials, TCMs fulfills this need. TCMs covers a wide array of materials that undergoes the reaction of AB + heat ↔ A+ B, some example of this "B" material includes, but not limited to

water, ammonia, hydroxide, oxide, etc.[6] This work focuses on TCMs with water reactions.[7] In the class of water-reacting TCMs, there exists adsorption materials (e.g. zeolites and silica gels),[5c, 7b] where the reversible reaction is based on weak van der Waals interactions between solid and gas (physisorption, energy density 100 to 200 kWh/m^3) and is limited to the surface of the solid, and absorption materials where energy is stored or released by reversible solid-gas reaction (chemisorption) which involves breaking and restoring strong bonds (such as covalent bonds) between the constituents throughout the bulk of the material. Consequentially, absorption materials such as inorganic salts ($SrCl_2 \cdot 6H_2O$, $MgSO_4 \cdot 7H_2O$, $K_2CO_3 \cdot 1.5H_2O$, etc.) which have their water bonded within the structure have higher energy densities (approximately 500 kWh/m^3) when compared to adsorption-based materials (approximately 200 kWh/m^3) as shown in Figure 1a. This work focuses on inorganic salt hydrate TCMs that are uniquely suited for on-site TES for buildings because apart from having high energy densities, they have negligible self-discharge and can be charged at temperatures below 100°C. Furthermore, since they are made from earth abundant materials, they are very economical. Figure 1b shows an example for the implementation of salt hydrates as TCM-thermal storage that can be charged using solar energy or excess grid electricity and discharged for thermal end-uses in buildings such as space and water heating by harvesting moist air from the surroundings.

Despite promising attributes of salt hydrates as TCMs, however, it is not widely used as TCMs but instead most of the research in these materials are limited to their use as PCMs.[8] One of the major issues with TCMs is its poor multi-cyclic efficiency,[9] with most of the research work showing significant drop in energy densities of salt hydrates just after 20 to 50 cycles. This drop is mainly related to material-level instabilities (pulverization, agglomeration, change in porosity, etc.) as salt hydrates undergo extreme volumetric changes during each thermal cycle. To accommodate these instabilities many studies have been done to create TCM composites to improve the structural integrity and stability for long-term cycling. Incorporation of certain host matrices into TCM composites also improve overall thermal and mass transport

properties.[10] Inert host matrices such as expanded graphite, vermiculite, silica gel, metal organic frameworks, etc. are often selected for these purpose.[11] Typically, a solution-based impregnation (wet) method is used to make TCM composites where the salt hydrate is turned into a saturated solution in water (overhydration past the deliquescence point) and the host matrix is added to this solution, where these materials may impregnate the nanopores of the host matrix.[12] Once homogenous slurry is achieved, it is then dried to make the TCM composite. This method, however, often results in agglomeration of salt hydrate particles during the drying process, which reduces the mass transport resulting in poor performance of the composite.[9b, 11e, 13] In this work, we explore the option of utilizing solid-state mixing to mitigate the issues incorporated with wet mixing. Solid-state mixing of salt hydrate with the inert matrix (dry mixing) is more desirable as it resolves the issue of agglomeration of salt hydrates and also significantly reduces the energy and cost associated with the drying step of the wet manufacturing process.[11c-e]

With dry mixing, the issue that is faced during cycling is the pulverization of the TCM salt hydrates. So far, many studies have reported the pulverization of TCMs with cycling,[11e, 14] but none have provided a mechanistic understanding and physical insights into predicting such behavior, i.e. whether the material will continue to pulverize or if there is a critical size below which the particle is stable. Efforts such as coating and encapsulation of salt hydrates; and embedding salts hydrates into inert matrices have been done to improve long-term performance and stability of the salt hydrates, however, mechanical instabilities of pristine salt with cycling are not investigated.[10a, 13, 15] In the dry mixing process, since the salt hydrates are not dissolved in the water, it is crucial to know the stable size (or critical size or pulverization limit) of salt-hydrates before making the composite to prevent massive structural changes in the composites during thermal cycling.

In typical salt hydrates, water can account for approximately 1/4 to 1/2 the mass of the salt hydrate itself. For example, in a commonly investigated salt TCM for building applications

such as $MgSO_4 \cdot 7H_2O$,[14f] water occupies approximately 51% of the salt hydrate's mass, this causes large volume and porosity change when water molecules are removed and reintroduced (approx. 71.8% volume reduction during dehydration).

Previous investigation of the transitions of TCM salt hydrates between various hydrate phases has shown that different salts may undergo different mechanisms during both dehydration and hydration. The hydration of salt can follow different pathways (i.e. a direct solid-solid transition or a dissolution and a recrystallization process),[5d, 16] however, salt dehydration for most salts are common with a diffusion of water molecules out of the salt hydrate crystal. Consequentially, this removal of water from the crystal induces a solid-state transformation and causes a degree of mechanical stress and strain on the crystal itself, causing defects (i.e. dislocation and formation of cracks)[17] that in the long run can result in the self-pulverization of salt. Thus, whilst both hydration and dehydration may contribute in the deterioration of salt hydrates over cycling due to the large morphological changes, dehydration is considered to be the largest contributor towards the pulverization of salt hydrate.

In this work, $SrCl_2 \cdot 6H_2O$ is chosen and investigated for building application as it has low charging temperature (<100°C) when compared to $MgSO_4 \cdot 7H_2O$, and higher stability owing to its higher deliquescence point. Figure 1c and S1 shows the effect of cycling on $SrCl_2 \cdot 6H_2O$ (in here, water accounts for 1/3 mass of the salt hydrate) where the particle size gets reduced from > 400 µm (as received) to < 10 µm after just 10 cycles. This 40-fold reduction in particle size creates significant change in the surface area of the salt hydrates and shift the dynamics of the reaction. Here, we developed a model to predict the pulverization limit (i.e., critical size, R_{crit}) of salt hydrates and validated it for various salt hydrates. We also demonstrated the effect of R_{crit} on the dehydration and hydration kinetics as well as provided insights into the long-term stability of salt hydrates and its composites.

2. Results and Discussion

To determine how much the salt hydrates will pulverize due to expansion during cycling, a theoretical model for a single spherical particle was developed by solving the coupled mechanical stress and mass diffusion equations. This model is developed based on the mechanical response of the particle to water generation (i.e. dehydration), which leads to internal expansion gradients within the particle core. To begin, we assume that the salt hydrate is a perfectly spherical, defect-free particle with isotropic material properties. As it will be shown, the results of the model do not depend strongly on material properties, but instead on the rate of dehydration. Thus, although a real salt hydrate is not perfectly spherical, and certainly does not have perfectly isotropic material properties, this assumption will be of little consequence to the final model predictions. First, we consider the well-known stress response due to thermal expansion within a sphere:

$$\sigma_{rr} = \frac{2E\alpha_T}{1-v}\left\{\frac{1}{R^3}\int_0^R \theta(r)r^2 dr - \frac{1}{r^3}\int_0^r \theta(r)r^2 dr\right\} (1)$$

$$\sigma_{\phi\phi} = \frac{E\alpha_T}{1-v}\left\{\frac{1}{r^3}\int_0^R \theta(r)r^2 dr - \frac{2}{R^3}\int_0^r \theta(r)r^2 dr - C(r)\right\} (2)$$

Where E is the Young's modulus, α_T is the linear coefficient of thermal expansion, v is the Poisson ratio, R is the radius of the sphere, and $\theta(r) = T(r) - T_o$, where T_o is the reference temperature. Equations [1] and [2] give the thermomechanical response to an arbitrary temperature gradient induced in a solid sphere at steady state. To get the mechanical response to water generation, we can write the mass transfer analogue of equations 1-2. First, we recognize that the strain gradient is induced via the dehydration reaction, which occurs volumetrically. Thus, the mass analogue to $\theta(r)$ corresponds to $C(r) - C_o$, where $C(r)$ is the number of water molecules at position r, and C_o is the reference number of dehydrated water molecules, which is equal to zero (e.g. the hydrated state). Next, we substitute α_T for α_{H_2O}, which represents the expansion per water molecule generated. Thus, when α_{H_2O} is multiplied with the expression in the brackets in equations 3-4, we are multiplying the expansion per water

molecule by the number of water molecules at position r, which gives us the strain. Multiplying

the strain by $\frac{E}{1-\nu}$ then yields the stress:

$$\sigma_{rr} = \frac{2E\alpha_m}{1-\upsilon}\left\{\frac{1}{R^3}\int_0^R C(r)r^2 dr - \frac{1}{r^3}\int_0^r C(r)r^2 dr\right\} (3)$$

$$\sigma_{\phi\phi} = \frac{E\alpha_m}{1-\upsilon}\left\{\frac{1}{r^3}\int_0^R C(r)r^2 dr - \frac{2}{R^3}\int_0^r C(r)r^2 dr - C(r)\right\} (4)$$

From equations 3-4, it is clear that the stress gradient is a function of the location within

the sphere. To evaluate equations 3-4, the distribution of water molecules generated throughout

the sphere must be known at steady state. This can be solved for using Fick's law, assuming

uniform mass (vapor) generation.

$$D_{ab}\nabla^2 C = N\frac{m'(t)}{M_{H_2O}} (5)$$

Where D_{ab} is diffusivity between the salt and the water vapor, $m'(t)$ represents the total

mass generation of water molecules within the sphere per second $[\frac{g}{s}]$, M_{H_2O} is the molar mass

of water, and N is Avogadro's number -- which makes the right-hand side describe the total

number of water molecules per second. Assuming the same 1D spherical geometry as in

equations 1-4, equation 5 can be readily solved by enforcing axisymmetry such that the gradient,

$C'(r = 0) = 0$, which caps vapor generation from blowing up at the center, and by setting the

concentration of water molecules at the sphere's boundary equal to the concentration of water

molecules in the air $C(R) = C_\infty$ (interface between the outermost shell and the environment at

equilibrium), which provides a "mass sink" to equation 5. The resulting profile of water

molecules is:

$$C(r) = \frac{Nm'R^2}{6D_{ab}}\left(1 - \frac{r^2}{R^2}\right) + C_\infty (6)$$

Equation 6 is then fed into the mechanical response equations (3 and 4) with an

assumption that salt hydrates' volume changes approximately 10% per water molecule when it

is calculated based on the mass change of salt hydrate during dehydration assuming constant

density (i.e. linear expansion coefficient becomes 0.1/3 = 0.033). To determine the critical

particle size, we first note that the principal stress in the azimuthal direction is always larger than in the radial direction, so we focus only on equation 4. By evaluating the integrals in equation 4 and solving for the position, r, that maximizes the stress, we can now determine the critical particle size (R_{crit}) by equating the maximum stress experienced by the sphere to the ultimate stress of the salt lattice. To be clear, R_{crit} defines the maximum size above which the particle will pulverize because of the internal stress due to salt contraction with water output will exceed the ultimate strength of the salt. The equation is as follows:

$$R_{crit} = 1.29 \left(\frac{\sigma_{yield} D_{ab} M_{H_2O}}{(1-\nu)\alpha_m ENm'(t)} \right)^{\frac{1}{5}} \quad (7)$$

Where σ_{yield} is yield strength of salt hydrate and M_{H_2O} is the molar mass of water. σ_{yield} values range from 15 MPa as the lower limit and 40 MPa as the higher limit for different salts hydrates,[18] D_{ab} is assumed to be approximately 10^{-6} cm²/s,[19], ν is Poisson's ratio (neglected due to insignificance to the overall result), α is approximated at 10^{-4} K^{-1} and E values are 5 GPa for the lower limit to 50 GPa as the higher limit.[18-20] The model predicts the mechanical response and failure condition of the salt hydrates based on their mechanical properties, coupled with diffusion rate and charge/discharge. Figure 2a shows the R_{crit} as a function of $m'(t)$ where both the lower and higher end of material constant values were taken into consideration to represent the range of mechanical and intrinsic properties for various salt hydrates.[18a, 18c, 19-20] Due to the nature of mass generation of water vapor during dehydration, the largest contributor of R_{crit} within this equation comes from the amount of H_2O within the salt hydrate and their mass generation rate ($m'(t)$).

This model is experimentally validated by testing various salt hydrates ($K_2CO_3 \cdot 1.5H_2O$, $MgSO_4 \cdot 7H_2O$, $SrCl_2 \cdot 6H_2O$ and $Na_3PO_4 \cdot 12H_2O$) under the similar testing conditions where different $m'(t)$ were generated as each salt hydrate had different molar mass of the water to lose in the same time window. Specifically, each salt hydrates were experimentally cycled between 25°C to 80°C and then rehydrated back at 25°C with 60% RH. The charging rate for all the

salts were kept constant at 1°C/min. The *m'(t)* was calculated based on the amount of water which are lost during the dehydration period. $K_2CO_3 \cdot 1.5H_2O$ and $Na_3PO_4 \cdot 12H_2O$ showed the most extreme behavior as the former only generates $1.5H_2O$ and the latter generates $12H_2O$ in a very short period of time.

As expected, the salt hydrates pulverized during cycling and significant reduction in particle size was observed for all the salt hydrates after 10 cycles (Figure 2b-e). The mean particle sizes for cycled salts correspond well with the R_{crit} predicted by the model as shown in Figure 2a. Although there is a size distribution for all salt hydrates after 10 cycles, it is anticipated that the larger particles ($>R_{crit}$) will continue to pulverize further with cycling until they reach the respective critical particle size as predicted by the model.

For a given salt hydrate, *m'(t)* can only be varied by changing operating conditions such as temperature ramp rate and/or relative humidity. Thus, we further investigated correlation between R_{crit} and *m'(t)* for $SrCl_2 \cdot 6H_2O$ under various operating conditions for different sized particles.

2.1. Correlation of Particle Size and m'(t)

To understand the effect of particle size on *m'(t)* in salt hydrates, multiple batches of $SrCl_2 \cdot 6H_2O$ in various sizes were prepared by ball milling and sieving (which will be referred here as pre-conditioning of salt) which allows for more control over particle size as opposed to self- pulverization of salt hydrates through cycling. As expected, the smaller size particles completed each of its transitions at lower temperature, whereas for larger ones there was a shift to higher temperature as shown in Figure S2. In other words, as opposed to 10 mins for smaller particles, it took 35 mins for the larger particles to complete the first transition ($6H_2O$ to $2H_2O$). Similarly, there was time lag for the second and third transitions based on size of the particle, but since these transitions happened at relatively high temperatures compared to the first transition, the effect of particle size on water transport kinetics was less significant (Figure S2).

Table S1 provides the transition temperatures of each hydrate forms for different average particle size.

From operational perspective, the time required to charge (dehydration) and discharge (hydration) thermal energy storage material is very critical, especially the discharge time as it determines the power density of the storage. Given that the transition steps are temperature and vapor pressure gated,[21] we investigated the effect of these variables by comparing the performance of the as-received salts (approximately 560.2 µm) with the pre-conditioned salt of size near R_{crit}. Figure 3a-c shows the effect of particle size on dehydration times with the increase in the temperature ramp rates, whereas larger particles require more time to dehydrate when compared to smaller particles at same ramp rates, indicating that the process is diffusion limited for larger particles. For small sized particles, mass generation rate increases linearly with the ramp rates reaching up to 826 g/s-m^3 (Figure 3c), indicating fast mass (water vapor) transport owing to large surface area. This similar behavior is also observed in the hydration process where dehydrated salt hydrates were rehydrated back to $6H_2O$ under different conditions of relative humidity and temperature (Figure 3d). Performing a size study on these salt hydrates as shown in Figure 3e results in a trend where larger salt hydrates take significantly longer to get back to its original mass with 6 molecules of water (approximately 150 min) whereas the pre-conditioned salts can reach it quite rapidly (approximately 60 min) under the same hydration conditions. In fact, by increasing the RH further it is possible to hydrate the small sized particles in 30 mins. Figure 3f displays the result of this faster reaction rate where the overall power density of the material improves significantly (227 kW/m^3 vs 630 kW/m^3 between the smallest and largest- sized particles).

As the relative humidity and/or temperature were increased, the hydration rate for small particles increased whereas large particles lagged behind owing to slower water transport. Thus, having the salt hydrates within the critical size not only allows for increased mechanical

stability but also provides more flexibility in parametric space of operations at the reactor level for both dehydration and hydration processes.

2.2. Self-Pulverization vs. Preconditioning of Salt Hydrate

Since the salt hydrates can be pre-conditioned or self-pulverized during initial cycling period to reach optimal size (R_{crit}), we investigated the effect of these two different approaches to achieve the R_{crit} on the performance of $SrCl_2 \cdot 6H_2O$. The first ten cycles of $SrCl_2 \cdot 6H_2O$ (as received) and preconditioned (10 µm) particle size are shown in Figure 4a-b. The shift in dehydration of as received $SrCl_2 \cdot 6H_2O$ is apparent in the thermogravimetric data, where the transition temperature continually shifts to lower temperature as the cycling continues for 10 cycles (Figure 4a). This is mainly due to improved kinetics (faster mass transport) due to self-pulverization of the salt hydrates resulting in smaller particles with increased surface area as the cycling happens. As expected, no significant shifts were observed in case of pre-conditioned salt (approximately 10 µm) as the particle size is already small enough and close to the R_{crit}, resulting in the steady kinetics. Please note this agrees with Figure S2 which also shows minimal difference between approximately 10 µm and 2.5 µm particles (approaching R_{crit}). The mass vs. time evolution (20 cycles) for these two samples are shown in Figure 4c-d. The difference in the change in dehydration and hydration times with cycling for as-received and pre-conditioned salt hydrate is highlighted in Figure 4e-h. Owing to large size distribution in the as received $SrCl_2 \cdot 6H_2O$, dehydration time for the first cycle for different batches of salt samples varied between 49 to 57 mins but nonetheless for all the batches tested, the dehydration time reduced significantly during initial cycling and stabilized at approx. 46 mins for the ramp up rate of 1°C/min. Overall, the energy density of 50 thermal cycles stays relatively constant with an average of 562.77 $\pm$ 4.89 kWh/m^3 (Figure S4). From XRD, it is seen that signature crystalline peaks of $SrCl_2 \cdot 6H_2O$ are apparent and present throughout cycling (Figure S5) suggesting stable sturcture.

For preconditioned salt, the dehydration time was steady between 44-46 mins. The larger contrast, however, comes from the differences in hydration behavior between the two (Figure 4g-h) where the hydration time for as-received salt hydrate continues to decrease in 20 cycles (from 127 mins to 107 mins) whereas the pre-conditioned salt experiences a constant hydration time (78 mins) in all cycle. The reason behind longer times for self- pulverized salt is the morphology of the as-received salt hydrate after 20 cycles, which looked different from preconditioned salts and resembled "pomegranate structure" which comprise of primary particles approximately 2.63 µm in size, stuck together as larger secondary particle size (similar pomegranate structure in battery electrode, see Figure S3).[22] Due to this hierarchal structure, the surface area of self-pulverized salt hydrates was smaller when compared to pre-conditioned salt hydrate and thus requires more hydration times (Figure 4g). Although Brunauer-Emmett-Teller (BET) analysis of self-pulverized salt hydrates also indicates an increase in both surface area and porosity with cycling (Figure S6), we anticipate that the surface area will continue to increase as the secondary particles break down further to primary particles and finally reaching similar surface areas as preconditioned salt hydrates.

Please note that the disparity between dehydration and hydration times (46 and 78 mins, respectively) for pre-conditioned salt can be explained through the different parameters required to induce the reactions. The dehydration of salt hydrates takes place at high temperature where reaction rates are higher whereas the hydration happens at low temperature (25°C) and is driven by a constant vapor pressure. As mentioned earlier and shown in Figure 3, both of these times can be controlled by varying appropriate parameters.

The preliminary results of our ongoing work for making TCM composites with pre-conditioned salt (Figure S7) shows that the composites made using pre-conditioned salt hydrates were mechanically intact and stable for >40 cycles as opposed to 20 cycles when the composites are made with as-received salt hydrates. These samples are continued to be cycled and display prolonged mechanical stability. Using preconditioned salts minimizes the formation

of cracks, slipping and changes in expansion/contraction behavior within the host matrix, this allows for a more predictable mechanical behavior during cycling which could result into better long-term performance of the composite TCMs.

3. Conclusion

This work demonstrates that model-based understanding of R_{crit} of salt hydrates that would be mechanically stable during cycling. This is very crucial as it provides not only pathways to make TCM composites using more energy efficient method of solid state (dry) mixing but also results in TCM composites which are more mechanically robust and have high multi-cyclic efficiency. Thus, predicting R_{crit} mitigates the one of the major limitations TCM composites that hinders their more general usage. Furthermore, reaching R_{crit} induces faster hydration and dehydration reactions, thus allowing for a broader parametric space for reactor design optimizations.

4. Experimental Section

Materials: Strontium chloride hexahydrate (99%), magnesium sulfate heptahydrate (99.5%), potassium carbonate sesquihydrate (99%), sodium phosphate dodecahydrate (98%) were purchased from Sigma-Aldrich. Expandable graphite flakes were purchased from Alfa Aesar.

Sample Preparation: Salt hydrates were either used as received or grinded into desirable particle size. Prepared salts were grinded using mortar and pestle and sieved using various grade sieves to achieve desirable particle size average.

Thermogravimetric Analysis (TGA) and Differential Scanning Calorimetry (DSC): Dehydration experiments were done using TGA/DSC SDT650 (TA Instruments). Prepared salt hydrates were placed in an open alumina crucible and then heated to 150°C at 1°C/min. Nitrogen purge gas at 100 ml/min was used throughout the run. Data was analyzed using the TA Instrument TRIOS software. Rehydration and cyclic runs were done using a DSC/TGA 3+

(Mettler Toledo) with a modular humidity generator (MHG, ProUmid) extension. Prepared salt hydrates were placed in an open aluminum sample pan, heated to 80°C at 1°C/min at 0%RH, then cooled down to 25°C at 5°C/min with 60 %RH at the end, the samples were then held at 25°C 60 %RH for 90 minutes. Data was analyzed using the Mettler Toledo Star-e software.

Scanning Electron Microscopy (SEM): JEOL 7500F SEM with EDS was used for microscopy analysis. Samples were deposited onto a carbon tape on the sample holder. 10 mm working distance at 15 kV 10 µA was used for most imaging needs. Spot size was increased to 20 µA for EDS analysis to enhance signal.

Supporting Information
Supporting Information is available from the Wiley Online Library or from the author.

References

[1]   a) P. Albertus, J. S. Manser, S. Litzelman, *Joule* **2020**, *4*, 21-32; b) M. A. Pellow, C. J. M. Emmott, C. J. Barnhart, S. M. Benson, *Energy Environ. Sci.* **2015**, *8*, 1938-1952.
[2]   The heat is on. *Nature Energy* **2016**, *1*, 16193.
[3]   A. Odukomaiya, J. Woods, N. James, S. Kaur, K. R. Gluesenkamp, N. Kumar, S. Mumme, R. Jackson, R. Prasher, *Energy Environ. Sci.* **2021**, *14*, 5315-5329.
[4]   a) A. Sharma, V. V. Tyagi, C. R. Chen, D. Buddhi, *Renew. Sust. Energ. Rev.* **2009**, *13*, 318-345; b) S. M. Hasnain, *Energy Convers. Manag.* **1998**, *39*, 1127-1138.
[5]   a) K. Johannes, F. Kuznik, J.-L. Hubert, F. Durier, C. Obrecht, *Appl. Energy* **2015**, *159*, 80-86; b) Y. Zhang, R. Wang, *Energy Storage Mater.* **2020**, *27*, 352-369; c) H.

Deshmukh, M. Maiya, S. S. Murthy, *Appl. Therm. Eng.* **2017**, *111*, 1640-1646; d) K. Linnow, M. Niermann, D. Bonatz, K. Posern, M. Steiger, *Energy Procedia* **2014**, *48*, 394-404.

[6]   a) R. Dunn, K. Lovegrove, G. Burgess, *Proceedings of the IEEE* **2012**, *100*, 391-400; b) C. Roßkopf, S. Afflerbach, M. Schmidt, B. Görtz, T. Kowald, M. Linder, R. Trettin, *Energy Convers. Manag.* **2015**, *97*, 94-102; c) B. Bulfin, J. Vieten, C. Agrafiotis, M. Roeb, C. Sattler, *J. Mater. Chem A* **2017**, *5*, 18951-18966.

[7]   a) K. E. N'Tsoukpoe, T. Schmidt, H. U. Rammelberg, B. A. Watts, W. K. L. Ruck, *Appl. Energy* **2014**, *124*, 1-16; bC. Barreneche, A. I. Fernández, L. F. Cabeza, R. Cuypers, *Energy Procedia* **2014**, *48*, 273-279.

[8]   a) X. Xu, H. Cui, S. A. Memon, H. Yang, W. Tang, *Energy Build.* **2017**, *156*, 163-172; bK. Shahbaz, I. AlNashef, R. Lin, M. Hashim, F. Mjalli, M. Farid, *Sol. Energy Mater. Sol. Cells* **2016**, *155*, 147-154; cX. Zhang, X. Li, Y. Zhou, C. Hai, Y. Shen, X. Ren, J. Zeng, *Energy Fuels* **2018**, *32*, 916-921.

[9]   a) A.-J. de Jong, F. Trausel, C. Finck, L. Van Vliet, R. Cuypers, *Energy procedia* **2014**, *48*, 309-319; b) W. Li, M. Zeng, Q. Wang, *Sol. Energy Mater. Sol. Cells* **2020**, *210*, 110509; c) P. A. J. Donkers, L. Pel, O. C. G. Adan, *J. Energy Storage* **2016**, *5*, 25-32.

[10]   a) R.-J. Clark, M. Farid, *Sol. Energy Mater. Sol. Cells* **2021**, *231*, 111311; b) T. Yan, T. Li, J. Xu, J. Chao, R. Wang, Y. I. Aristov, L. G. Gordeeva, P. Dutta, S. S. Murthy, *ACS Energy Lett.* **2021**, *6*, 1795-1802.

[11]   a) J. Zhu, C. Gao, F. Kong, K. Zhang, Z. Bai, J. Guo, *Sol. Energy Mater. Sol. Cells* **2021**, *229*, 111118; b) P. D'Ans, E. Courbon, A. Permyakova, F. Nouar, C. Simonnet-Jégat, F. Bourdreux, L. Malet, C. Serre, M. Frère, N. Steunou, *J. Energy Storage* **2019**, *25*, 100881; c) H. Ait Ousaleh, S. Sair, S. Mansouri, Y. Abboud, A. Faik, A. El Bouari, *Sol. Energy Mater. Sol. Cells* **2020**, *215*, 110601; d) H. Zhou, D. Zhang, *Sol. Energy* **2019**, *184*, 202-208; eA. I. Shkatulov, J. Houben, H. Fischer, H. P. Huinink, *Renew. Energy* **2020**, *150*, 990-1000.

[12]   a) J. Xu, T. Li, J. Chao, S. Wu, T. Yan, W. Li, B. Cao, R. Wang, *Angew. Chem. Int. Ed.* **2020**, *59*, 5202-5210; b) J. Xu, T. Li, T. Yan, S. Wu, M. Wu, J. Chao, X. Huo, P. Wang, R. Wang, *Energy Environ. Sci.* **2021**, *14*, 5979-5994.

[13]   R.-J. Clark, A. Mehrabadi, M. Farid, *J. Energy Storage* **2020**, *27*, 101145.

[14]   a) L. C. Sögütoglu, P. A. J. Donkers, H. R. Fischer, H. P. Huinink, O. C. G. Adan, *Appl. Energy* **2018**, *215*, 159-173; b) M. Stanish, D. Perlmutter, *AIChE journal* **1984**, *30*, 56-62; c) R. Fisher, Y. Ding, A. Sciacovelli, *J. Energy Storage* **2021**, *38*, 102561; d) P. A. Kallenberger, K. Posern, K. Linnow, F. J. Brieler, M. Steiger, M. Fröba, *Adv. Sustainable Syst.* **2018**, *2*, 1700160; e) P. A. J. Donkers, S. Beckert, L. Pel, F. Stallmach, M. Steiger, O. C. G. Adan, *J. Phys. Chem. C* **2015**, *119*, 28711-28720; f) V. Van Essen, H. Zondag, J. Gores, L. Bleijendaal, M. Bakker, R. Schuitema, W. Van Helden, Z. He, C. Rindt, *J. Sol. Energy Eng.* **2009**, *131*.

[15]   a) A. Shkatulov, R. Joosten, H. Fischer, H. Huinink, *ACS Appl. Energy Mater.* **2020**, *3*, 6860-6869; b) M. Graham, J. Smith, M. Bilton, E. Shchukina, A. A. Novikov, V. Vinokurov, D. G. Shchukin, *ACS Nano* **2020**, *14*, 8894-8901; c) V. Mamani, A. Gutiérrez, S. Ushak, *Sol. Energy Mater. Sol. Cells* **2018**, *176*, 346-356.

[16]   L.-C. Sögütoglu, M. Steiger, J. Houben, D. Biemans, H. R. Fischer, P. Donkers, H. Huinink, O. C. G. Adan, *Cryst. Growth Design* **2019**, *19*, 2279-2288.

[17]   S. Chizhik, A. Matvienko, A. Sidelnikov, *Cryst. Eng. Comm.* **2018**, *20*, 6005-6017.

[18]   a) V. Kanchana, G. Vaitheeswaran, A. Svane, *J. Alloys Compd.* **2008**, *455*, 480-484; b) A. D. Fortes, K. S. Knight, I. G. Wood, *Acta Crystallogr. B* **2017**, *73*, 47-64; c) P. M. Grindrod, M. J. Heap, A. D. Fortes, P. G. Meredith, I. G. Wood, F. Trippetta, P. R. Sammonds, *J. Geophys. Res.* **2010**, *115*.

[19]   J. Ding, L. Du, G. Pan, J. Lu, X. Wei, J. Li, W. Wang, J. Yan, *Appl. Energy* **2018**, *220*, 536-544.

[20]   a) H. Lauer Jr, K. Solberg, D. Kühner, W. Bron, *Phys. Lett. A* **1971**, *35*, 219-220; b) H. Ghaedi, M. Ayoub, S. Sufian, A. M. Shariff, B. Lal, C. D. Wilfred, *J. Chem. Thermodyn.* **2018**, *118*, 147-158.

[21]   M. Steiger, *J. Chem. Thermodyn.* **2018**, *120*, 106-115.

[22]   a) N. Liu, Z. Lu, J. Zhao, M. T. McDowell, H.-W. Lee, W. Zhao, Y. Cui, *Nat. Nanotechnol.* **2014**, *9*, 187-192; b) Q. Xu, J. Y. Li, J. K. Sun, Y. X. Yin, L. J. Wan, Y. G. Guo, *Adv. Energy Mater.* **2017**, *7*, 1601481; c) T. Shen, X.-h. Xia, D. Xie, Z.-j. Yao, Y. Zhong, J.-y. Zhan, D.-h. Wang, J.-b. Wu, X.-l. Wang, J.-p. Tu, *J. Mater. Chem A* **2017**, *5*, 11197-11203.
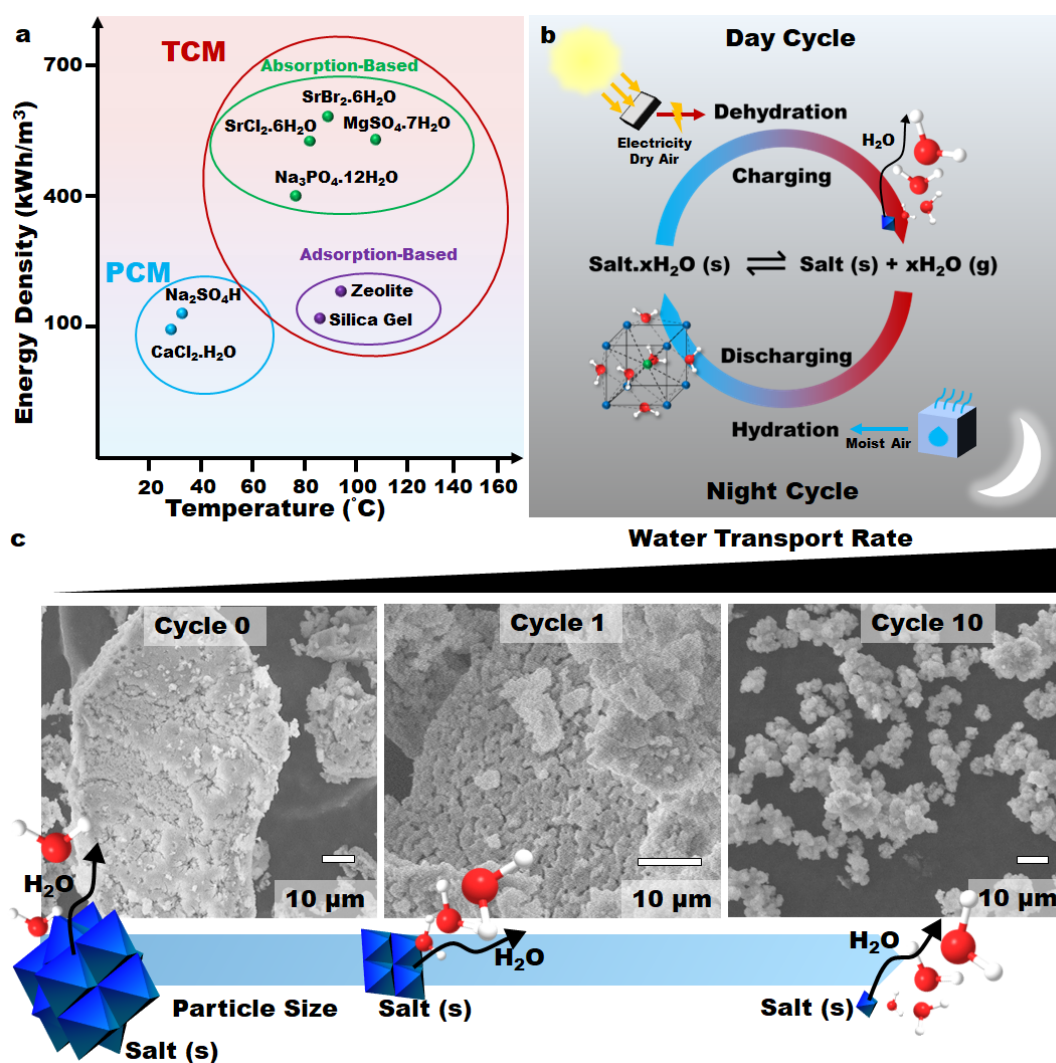
Figure 1. (a) Energy density comparison between various thermal energy storage materials including phase change materials (PCM), water-based adsorption and absorption thermochemical materials (TCM). (b) Illustration for use of TCMs in buildings and charge-discharge cycle of salt hydrates where the salt hydrates can be dehydrated using the energy generated through solar power and then rehydrated at night with outside humid air or a humidifier. (c) SEM image and illustration of the change in salt hydrate ($SrCl_2.6H_2O$) morphology and size during cycling.

16
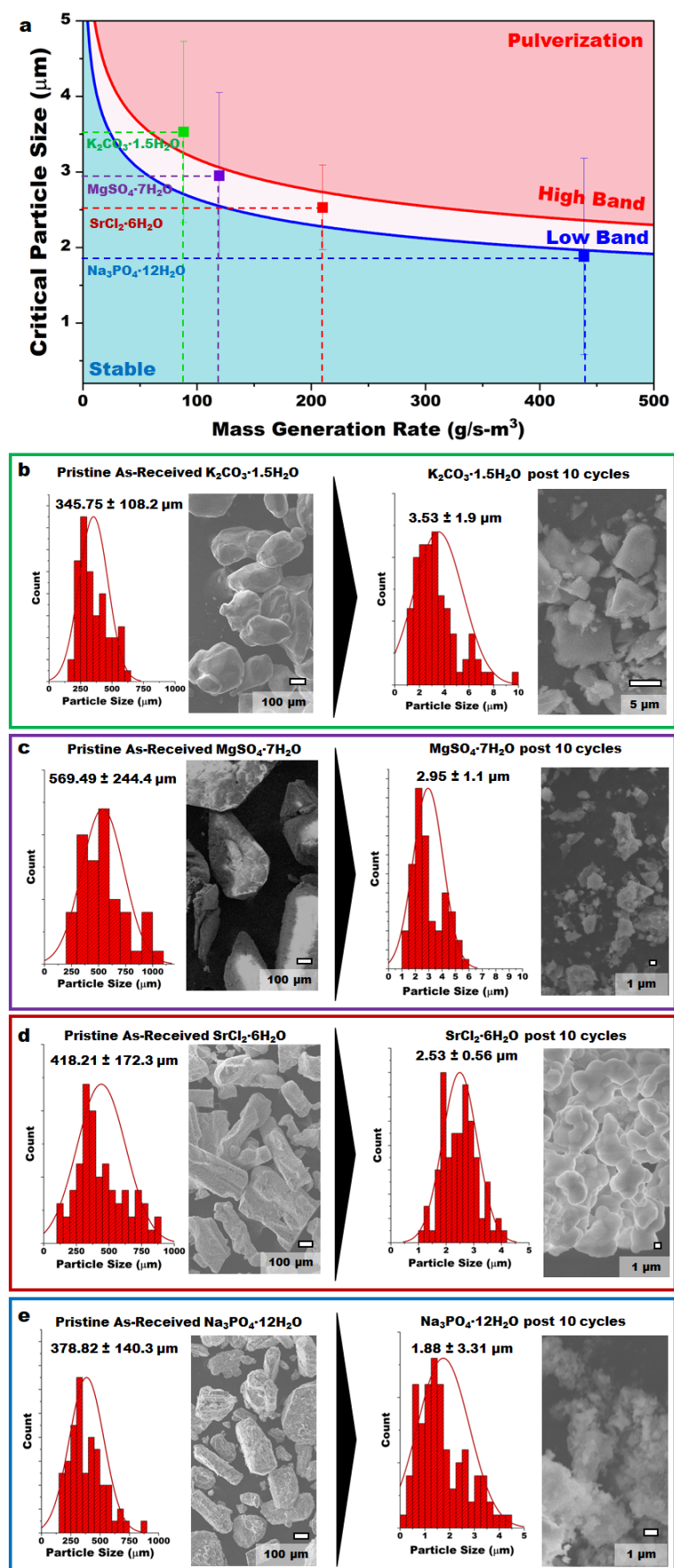
Figure 2. (a) Model along with experimental data on the critical particle size of salt hydrates. Two set of material constant values were taken to represent the range of mechanical and

intrinsic properties for various salt hydrates. Size distribution and SEM image for pristine (as received) to post 10 cycles of (b) $K_2CO_3.1.5H_2O$ (c) $MgSO_4.7H_2O$, (d) $SrCl_2.6H_2O$, and (e) $Na_3PO_4.12H_2O$. Cycling was done between 25°C, 60% RH and 80°C, 0% RH at 1°C/min ramp rates.
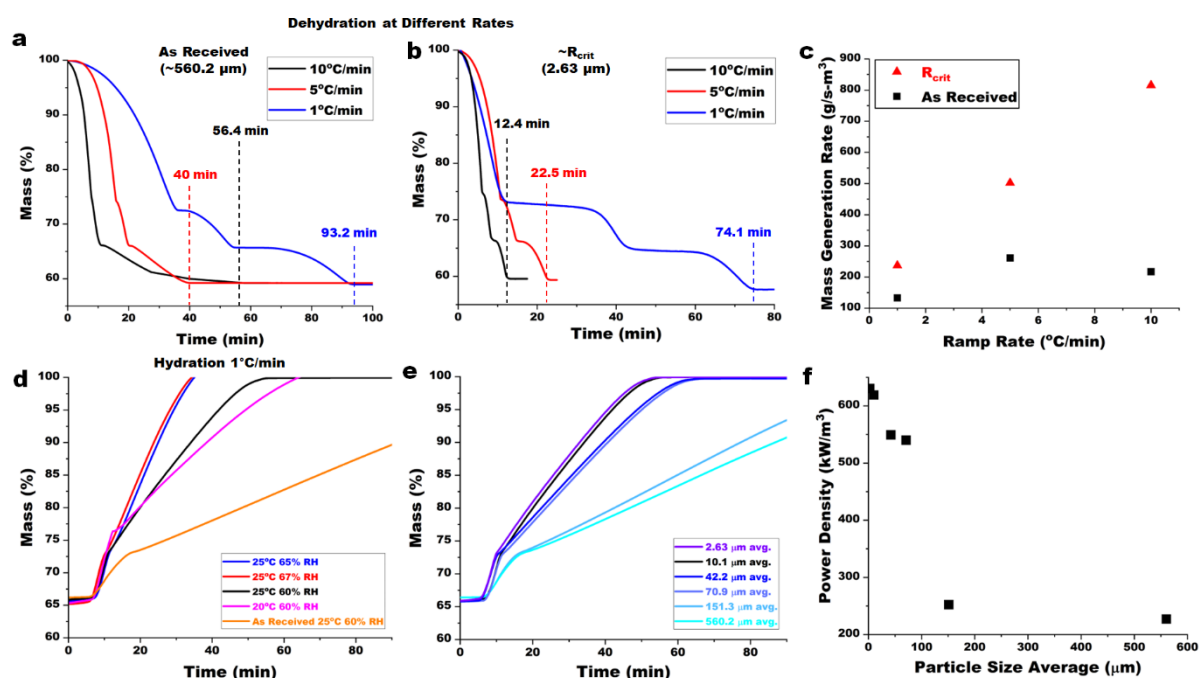
Figure 3. Dehydration and hydration behavior of $SrCl_2.6H_2O$ with various average starting size and ramp rates. (a) Dehydration time from $6H_2O$ to anhydrous of as-received particles at various temperature ramp rates. (b) Dehydration time from $6H_2O$ to anhydrous of pre-conditioned particles close to R_{crit} at various temperature ramp rates. (c) Relation between mass generation rate and ramp rates for as received and pre-conditioned particles. (d) Hydration times for pre-conditioned and as-received particles with different temperature and relative humidity conditions. (e) Hydration times for particles with different initial sizes. (f) Effect of particle size on power density.
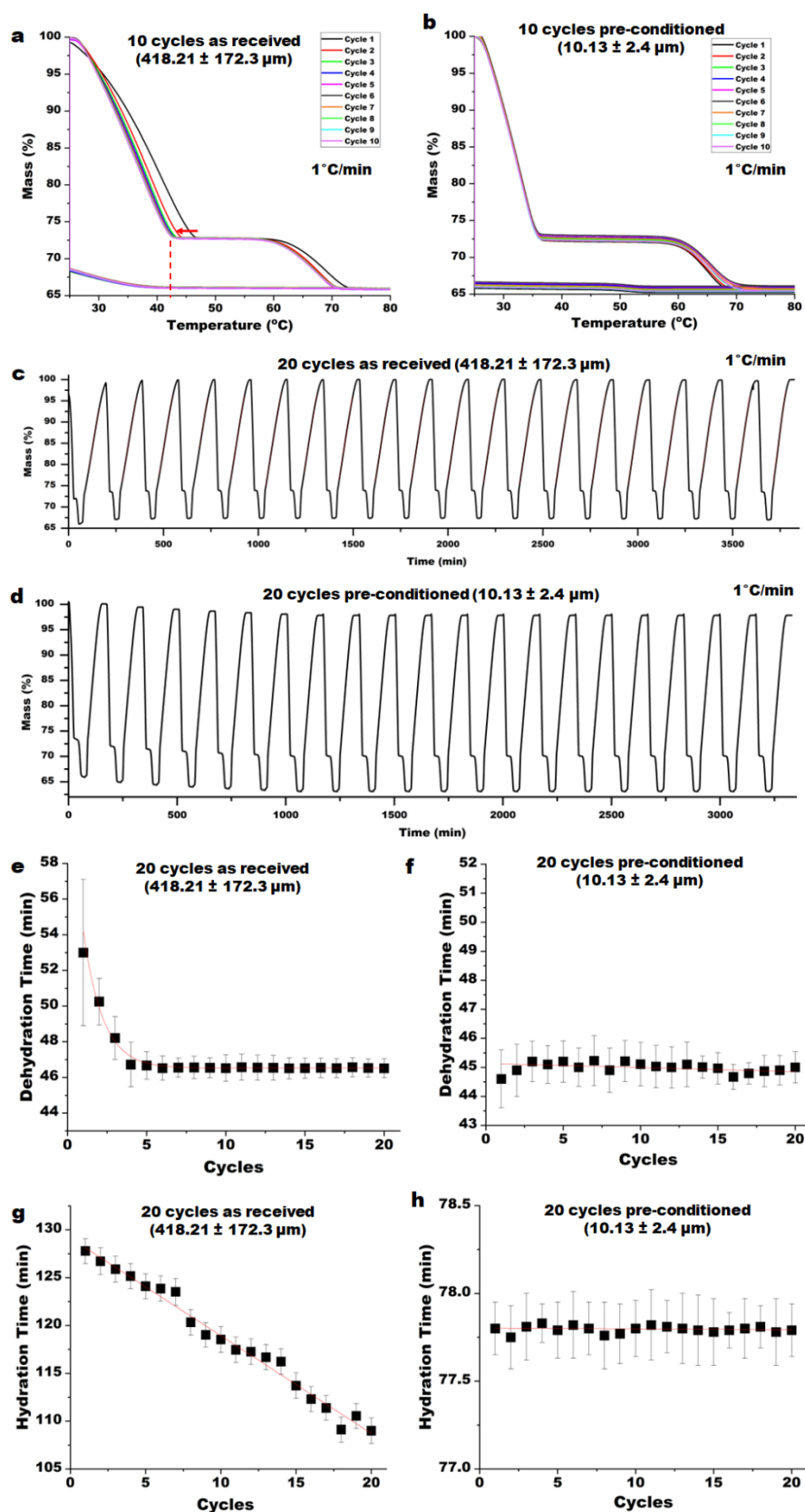
Figure 4. Gravimetric data of (a) as-received $SrCl_2.6H_2O$ and (b) pre-conditioned $SrCl_2.6H_2O$ cycled 10 times. Mass vs. time evolution of (c) as received $SrCl_2.6H_2O$ and (d) pre-conditioned $SrCl_2.6H_2O$ cycled 20 times at 1°C/min between 25°C, 60% RH and 80°C, 0% RH. Change in dehydration time for (e) as-received $SrCl_2.6H_2O$ and (f) pre-conditioned

$SrCl_2.6H_2O$. Change in hydration time for (g) as-received $SrCl_2.6H_2O$ and (h) pre-conditioned $SrCl_2.6H_2O$.